Heliyon

ELSEVIER

Received:
12 October 2018
Revised:
11 December 2018
Accepted:
30 January 2019

Cite as: M. A. Islam, M. Zahidur Rahaman, Md. Mehedi Hasan, A. K. M. Akther Hossain. Analysis of grain growth, structural and magnetic properties of Li-Ni-Zn ferrite under the influence of sintering temperature. Heliyon 5 (2019) e01199. doi: 10.1016/j.heliyon.2019.e01199

Analysis of grain growth, structural and magnetic properties of Li-Ni-Zn ferrite under the influence of sintering temperature

M. A. Islam [a,*], **M. Zahidur Rahaman** [b,**], **Md. Mehedi Hasan** [c], **A. K. M. Akther Hossain** [b]

[a] *Department of Physics, University of Barisal, Barisal 8200, Bangladesh*

[b] *Department of Physics, Bangladesh University of Engineering and Technology, Dhaka, Bangladesh*

[c] *Bangladesh Atomic Energy Commission, Dhaka 1000, Bangladesh*

[*] Corresponding author.

[**] Corresponding author.

E-mail addresses: arifphy6@gmail.com (M.A. Islam), zahidur.physics@gmail.com (M.Z. Rahaman).

Abstract

The effect of sintering temperature (T_S) on the structural and magnetic properties of $Li_{0.15}Ni_{0.3}Zn_{0.4}Fe_{2.15}O_4$ is investigated and discussed. The sample is synthesized by the sol-gel auto combustion method and sintered at 1373−1573 K for 5 h. Phase identification of the powder sample was performed by using the X-ray diffraction (XRD). The XRD patterns confirmed the formation of single phase cubic spinel structure. The bulk density is correlated with T_S. From the energy-dispersive X-ray spectroscopy study, it is observed that the percentage of the elements in the component phases is well consistent with the nominal composition of the composites. Field Emission Scanning Electron Microscopy showed that the average grain size (D) is increased with increasing T_S. The frequency (100 Hz−120 MHz) dependent complex initial permeability spectra and relative quality factor increased with sintering temperature up to 1523 K then decreased for further increase in temperature. The complex initial

https://doi.org/10.1016/j.heliyon.2019.e01199

permeability has been explained with the help of microstructure, and the redistribution of cations in their sites.

Keywords: Condensed matter physics, Materials science

1. Introduction

Ferrite is a very important class of magnetic materials from the application point of view and is extensively used as permanent magnets in market because of their low price and high magnetic performance [1]. The physical properties of ferrite are related to the structure of solid. They belong to a large class of compounds which have a spinel type structure. The spinel type unit cell consists of a cubic array of 32 oxygen anions, 16 Fe^{3+} ions and 8 Fe^{2+} ions. A total of 24 metal cations are distributed among 8 tetrahedral interstices and 16 octahedral interstices [2, 3]. Lithium ferrites form an important class of materials exhibiting high Curie temperature, high resistivity, high saturation magnetization etc. They are used in various device applications such as telecommunication and microwave device [4, 5, 6, 7]. Recently, with the development of telecommunications, ferrites with high permeability and high frequency stability are widely used to produce all kinds of broadband elements. For developing inductors, transformers, and RF components, which are operating at a high frequency range, soft magnetic nano-composite cores are being improved day by day [8, 9, 10]. Many compositions of this ferrite contain a high quantity of nonmagnetic Zn ferrite; it leads to the decrease of Curie temperature and thermo stability [11].

Recently Islam *et al* investigated the detailed magnetic properties of Zn substituted Li-Ni-ferrite [12]. After Zn substitution the initial permeability is enhanced and loss factor is decreased at a considerable amount. They studied different magnetic parameters with respect to the Zn content. However, sintering temperatures have significant effect on the structural and magnetic properties of materials. Hence, it is also necessary to understand the variation of magnetic properties with respect to the sintering temperature. In this research we are interested to investigate the effect of various T_S on the structural and magnetic properties of $Li_{0.15}Ni_{0.3}Zn_{0.4}Fe_{2.15}O_4$.

2. Experimental

2.1. Sample synthesis technique

By using the sol-gel auto combustion technique $Li_{0.15}Ni_{0.3}Zn_{0.4}Fe_{2.15}O_4$ sample was prepared. We have used citric acid, $LiNO_3$, $Ni(NO_3)_2.6H_2O$, $Zn(NO_3)_2.6H_2O$, and $Fe(NO_3)_3.9H_2O$ as raw materials. For making solution, particular amount of citric acid and nitrates were dissolved into distilled water. The molar ratio between

https://doi.org/10.1016/j.heliyon.2019.e01199

citric acid and metals was 1:3. By using ammonia solution the P^H of the solution was kept fixed at about 7. In the next step the solution was heated at about 360 K for several hours. A magnetic stirrer was used to stir the solution during the procedure. After the whole process, dense gel form of the solution was obtained. Finally, the fluffy nano-sized loose powder was obtained from the gel form of the solution. Then by using PVA (Polyvinyl Alcohol) the fine powders are granulated and pressed into toroid shaped and disk shaped samples. The schematic diagram of the sample preparation technique is illustrated in Fig. 1. The samples are then sintered at different temperatures (1373, 1423, 1473, 1523 and 1573 K) for about 5 hours.

2.2. Characterization

An X-ray diffractometer (CuK_α as a target and $\lambda = 0.1540598$ nm) was used for the structural characterization of the studied samples. Nelson-Riley function [13] was used for evaluating the lattice parameters of the composition given in Eq. (1).

$$F(\theta) = \frac{1}{2}\left[\frac{\cos^2\theta}{\sin\theta} + \frac{\cos^2\theta}{\theta}\right] \tag{1}$$

Where θ is defined as the Bragg's angle. The theoretical density (ρ_{th}) was computed by using Eq. (2).

$$\rho_{th} = \frac{8M_A}{N_A a_0^3} \tag{2}$$

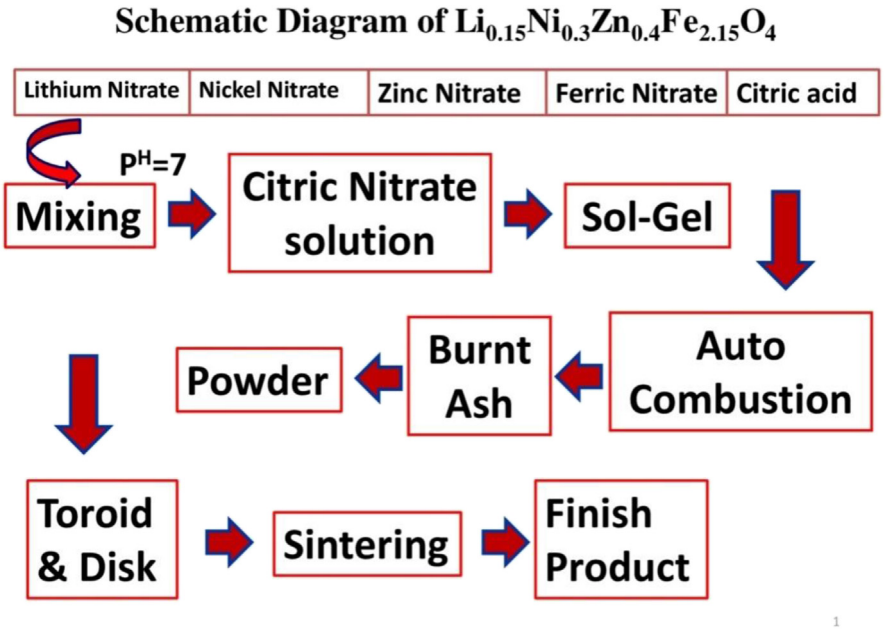

Fig. 1. Schematic diagram of the sample preparation.

https://doi.org/10.1016/j.heliyon.2019.e01199

where N_A stands for the Avogadro's number, M_A defines the molecular weight of the composition and a_0 is the lattice constant. The bulk density, ρ_B, of the samples was determined by using Eq. (3).

$$\rho_B = \frac{M}{\pi r^2 t} \tag{3}$$

where M is the mass of the sample, r is the radius and t is the thickness of the pellet. The porosity (P) was evaluated from the relation given in Eq. (4).

$$P(\%) = \frac{\rho_{th} - \rho_B}{\rho_{th}} \times 100 \tag{4}$$

where ρ_B is the bulk density. FESEM (Field Emission Scanning Electron Microscopy) was used for studying the microstructure and surface morphology of the studied samples. By using the linear intercept technique [14] average grain size of the samples were evaluated. For studying the frequency dependent initial permeability of $Li_{0.15}Ni_{0.3}Zn_{0.4}Fe_{2.15}O_4$ ferrite Wayne Kerr Impedance Analyzer was used. The complex initial permeability measurements have been performed in the frequency range 100 Hz−120 MHz at room temperature.

The real part of the complex initial permeability ($\mu_i^{/}$) have been evaluated by using Eq. (5).

$$\mu_i^{/} = \frac{L_s}{L_0}, \tag{5}$$

where L_s defines the self-inductance of the sample core and the inductance of the winding coil without the sample core is given by Eq. (6) [15].

$$L_o = \frac{\mu_o N^2 S}{\pi d} \tag{6}$$

Where S is the area of cross section, N is the number of turns of the coil (N = 4), and the mean diameter can be calculated by using Eq. (7).

$$d = \left(\frac{d_i + d_o}{2}\right) \tag{7}$$

where d_i and d_0 stands for the inner and outer diameter of the toroidal sample, respectively. The relative quality factor (RQF) is computed from the relation given in Eq. (8) [16].

$$RQF = \frac{\mu_i^{/}}{\tan \delta} \tag{8}$$

https://doi.org/10.1016/j.heliyon.2019.e01199

3. Results and discussion

3.1. Crystal structure, lattice parameter, density and porosity

The XRD patterns of $Li_{0.15}Ni_{0.3}Zn_{0.4}Fe_{2.15}O_4$ for both ash burnt nano powder and sintered bulk powder are shown in Fig. 2. A slightly broader peak for ash burnt nano powder [Fig. 2(a)] indicates the formation of nano-sized particles. The crystallite size of this composition is evaluated by using the (311) diffraction peak by the Scherer formula [2] as shown in Fig. 3(a). The calculated value of the crystallite size is 27 nm. The FESEM image of this as grown powder [Fig. 3(b)] indicates that the nano-sized powder is spherical in shape and uniformly distributed. Fig. 2(b) illustrates the XRD patterns of $Li_{0.15}Ni_{0.3}Zn_{0.4}Fe_{2.15}O_4$ sintered at 1523 K. Sharp and well defined intense peaks are observed, indexed as (111), (220), (311), (222), (400), (422), (511) and (440). The XRD pattern confirms that all compositions have single phase cubic spinel structure. Though the Ash-burnt nano powder contains one impurity peak, the sintered bulk powder have no impurity peak as all the peaks in pattern matched well with characteristic reflections of earlier reported spinel ferrites [17].

The lattice parameter of the sample is plotted against Nelson-Riley function F(θ) in Fig. 4. The lattice constant, density, porosity (P), average grain size, natural resonance frequency, maximum quality factor and initial permeability of $Li_{0.15}Ni_{0.3}Zn_{0.4}Fe_{2.15}O_4$ are presented in Table 1. The ρ_B of the $Li_{0.15}Ni_{0.3}Zn_{0.4}Fe_{2.15}O_4$ sample is increased with the increase in T_S from 1373 to 1523 K and above 1523 K, the density is decreased gradually. On the other hand, porosity (P) of the sample is decreased with the increase in T_S up to 1523 K. The increase in ρ_B with T_S is expected. This is because during the sintering process, the thermal energy generates a force that drives the grain boundaries to grow over pores, thereby decreasing the pore volume and denser the material. At higher T_S (1573 K) the ρ_B decreases because of the increase in

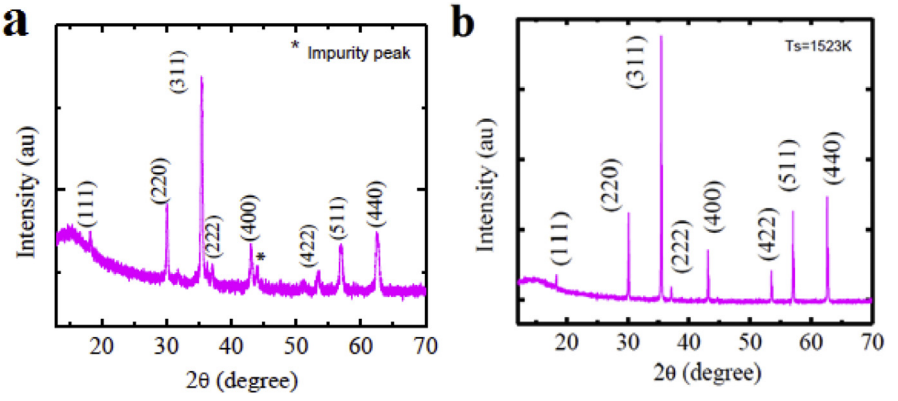

Fig. 2. The X-ray diffraction pattern for powder of $Li_{0.15}Ni_{0.3}Zn_{0.4}Fe_{2.15}O_4$. (a) Ash-burnt nano powder (b) Sintered bulk powder.

https://doi.org/10.1016/j.heliyon.2019.e01199

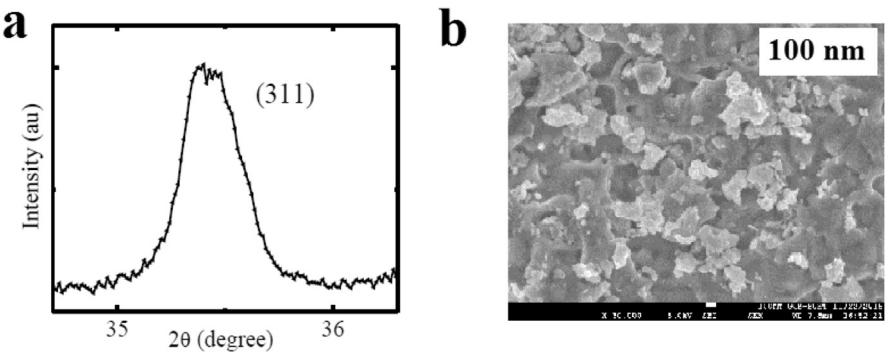

Fig. 3. The XRD pattern for (311) peak (a) and FESEM image (b) of as prepared powder sample $Li_{0.15}Ni_{0.3}Zn_{0.4}Fe_{2.15}O_4$.

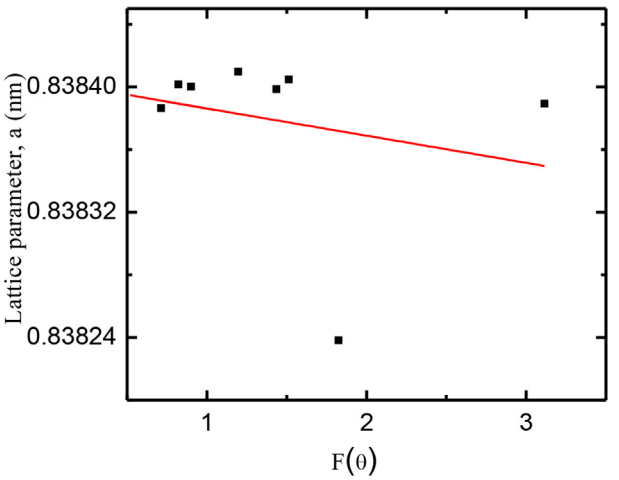

Fig. 4. The Nelson-Riley function F(θ) vs lattice parameter of $Li_{0.15}Ni_{0.3}Zn_{0.4}Fe_{2.15}O_4$.

intragranular P resulting from exaggerated grain growth as shown in Fig. 5. When the grain growth rate is very high, pores may be left behind by the rapidly moving grain boundaries, resulting in pores that are trapped inside the grains. The discontinuous growth of grain rises with temperature and hence contributing toward the reduction of the bulk density.

Table 1. The lattice constant, density, porosity, average grain size, natural resonance frequency, maximum quality factor and initial permeability of the $Li_{0.15}Ni_{0.3}Zn_{0.4}Fe_{2.15}O_4$ sintered at various T_s.

x	T_s *(K)*	a_o *(nm)*	$P_{th} \times 10^3$ *(Kg/m^3)*	$\rho_B \times 10^3$ *(Kg/m^3)*	*P* (%)	Average *grain size (μm)*	f_r *(MHz)*	RQF_{max}	μ_i' (at 1 MHz)
$Li_{0.15}Ni_{0.3}Zn_{0.4}Fe_{2.15}O_4$	1373	0.83840	5.16	4.57	11	1.77	90	7281	123
	1423			4.62	10	2.04	79	7238	126
	1473			4.76	7	2.90	22	11999	219
	1523			4.90	5	6.39	17	12395	250
	1573			4.79	7	10.52	15	11737	232

https://doi.org/10.1016/j.heliyon.2019.e01199

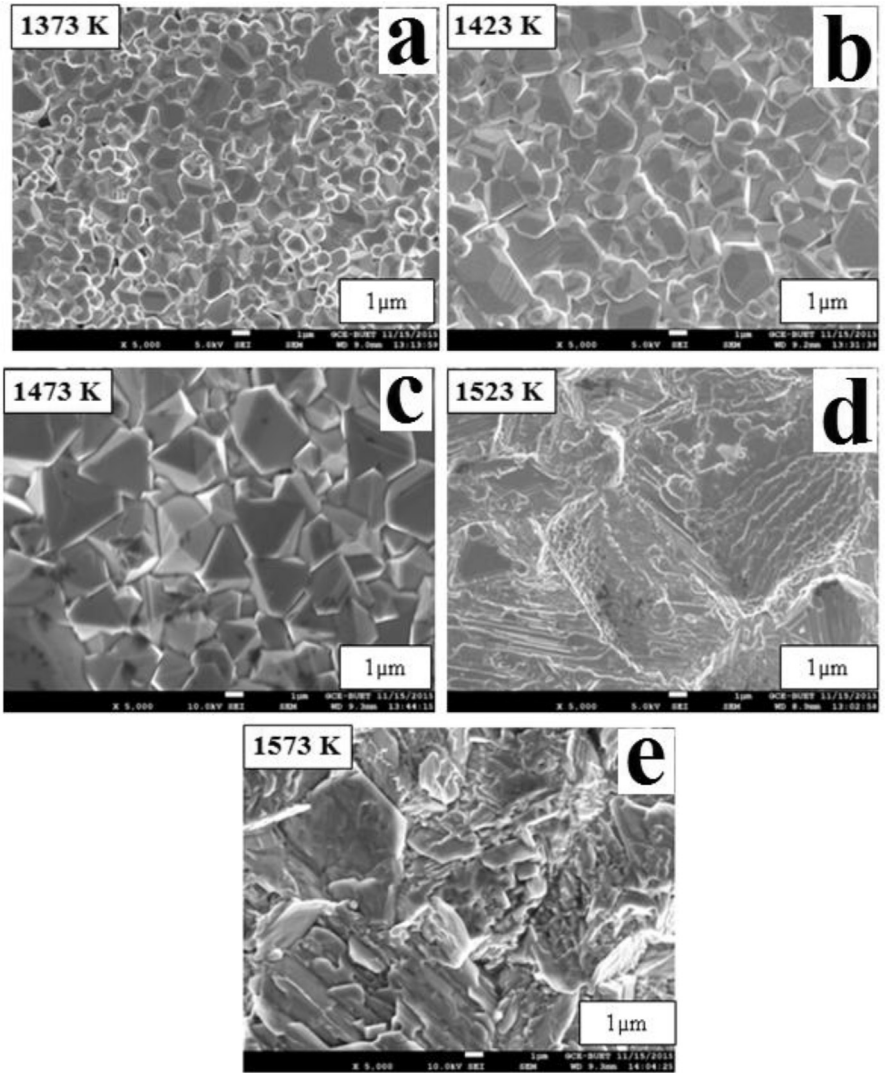

Fig. 5. The FESEM micrographs of $Li_{0.15}Ni_{0.3}Zn_{0.4}Fe_{2.15}O_4$ sintered at (a) 1373, (b) 1423, (c) 1473, (d) 1523 and (e) 1573 K.

3.2. Microstructure and EDS analysis

The typical FESEM micrograph of $Li_{0.15}Ni_{0.3}Zn_{0.4}Fe_{2.15}O_4$ sintered at various T_S are shown in Fig. 5. The grain size is significantly increased with the increase in T_S. The values of D for various samples are presented in Table 1. The uniformity in the grain size and average D can control materials properties such as the magnetic permeability. The behavior of grain growth reflects the competition between the driving force for grain boundary movement and the retarding force exerted by the pores [18].

The energy dispersive spectroscopy (EDS) of $Li_{0.15}Ni_{0.3}Zn_{0.4}Fe_{2.15}O_4$ is collected from FESEM to determine the composition at various T_s for 5 hours. Fig. 6 shows the obtained peaks correspond to Ni, Zn, Fe and O which forms the

https://doi.org/10.1016/j.heliyon.2019.e01199

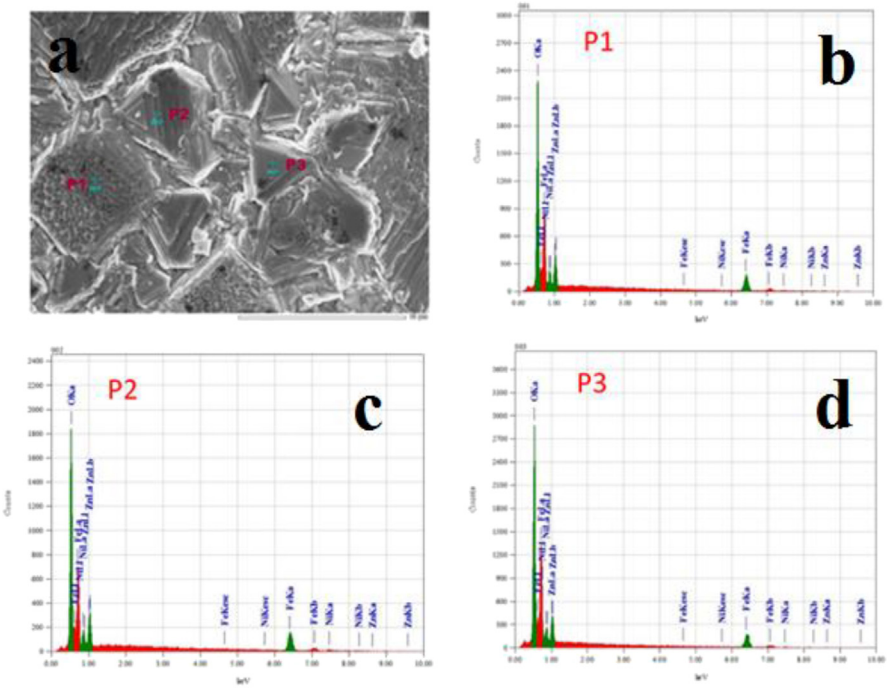

Fig. 6. (a) The micrograph of $Li_{0.15}Ni_{0.3}Zn_{0.4}Fe_{2.15}O_4$ sintered at 1523 K, (b) The EDS spectrum for P1 grain, (c) The EDS spectrum for P2 grain and (d) The EDS spectrum for P3 grain.

$Li_{0.15}Ni_{0.3}Zn_{0.4}Fe_{2.15}O_4$ sintered at 1523 K. On the other hand, Li has no definite peak because Li is light element and so it can not be routinely analyzed by EDS. The EDS confirms the present of all the constituent elements in the composition. There is no any impurity index in the composition. EDS also confirms the homogeneous distribution of the constituent elements. It is observed from the EDS spectrum that the percentage of the elements in the component phases is well consistent with the nominal composition of the phases in the ferrite materials [19]. Almost similar percentage of the elements is found in other nominal composition at various T_s.

3.3. Complex initial permeability

Fig. 7 shows the complex initial permeability spectra for $Li_{0.15}Ni_{0.3}Zn_{0.4}Fe_{2.15}O_4$ sample sintered at 1373, 1423, 1473, 1523 and 1573 K. It is observed that the real part of initial permeability ($\mu_i^{/}$) of $Li_{0.15}Ni_{0.3}Zn_{0.4}Fe_{2.15}O_4$ increases with increasing T_S up to 1523 K and above this a decreasing trend is observed as shown in Fig. 7. With the increase in sintering temperature pores and voids are reduced gradually. The permeability decreases above 1523 K because the sample heated at higher Ts (above optimum Ts) contains increasing number of pores within the grains which results a decrease in permeability. From Table 1 it is found that the resonance frequency (f_r) is decreased with the increase in sintering temperature, which is the

https://doi.org/10.1016/j.heliyon.2019.e01199

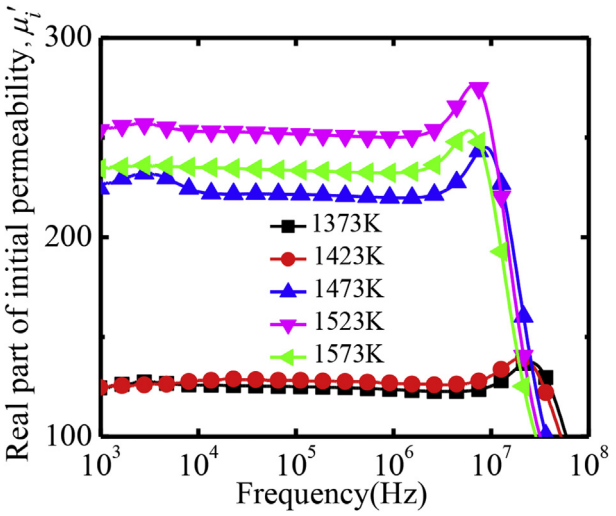

Fig. 7. The variation of μ'_i spectra for $Li_{0.15}Ni_{0.3}Zn_{0.4}Fe_{2.15}O_4$ with sintered at different temperatures.

desired property of ferrites. An inversely proportional relation of $\mu_i^{/}$ with f_r confirms the Snoek's limit [20]. The permeability of the polycrystalline ferrite is related to the two different magnetization mechanics: spin rotation and domain wall motion [21, 22, 23], which can be described by using Eq. (9).

$$\mu_i = 1 + \chi_w + \chi_{spin}, \tag{9}$$

where χ_w is the domain wall susceptibility given in Eq. (10); χ_{spin} is intrinsic rotational susceptibility given in Eq. (11).

$$\chi_w = \frac{3\pi M_s^2 D}{4\gamma} \tag{10}$$

$$\chi_{spin} = \frac{2\pi M_s^2}{K} \tag{11}$$

where M_s is the saturation magnetization, K is the anisotropy constant, D is the average grain diameter, and γ is the domain wall energy. The domain wall motion is influenced by the average grain size and enhanced with the increase in grain size. The loss factor, tanδ is increased with the increase in sintering temperature. The increase in sintering temperature results in increased loss in the sample, thereby creating defects in the lattice, which gives rise to the magnetic loss.

Fig. 8 shows the variation of RQF with frequency of $Li_{0.15}Ni_{0.3}Zn_{0.4}Fe_{2.15}O_4$ sintered at various T_S. The RQF gradually increases with increasing Ts up to 1523 K and above this the RQF founds to decrease as illustrated in Fig. 9. Abnormal grain growth is occurred which creates trapped pores inside the grain. This increasing amount of pores influences the loss factor and turns into the higher value which results a lower value of RQF.

https://doi.org/10.1016/j.heliyon.2019.e01199

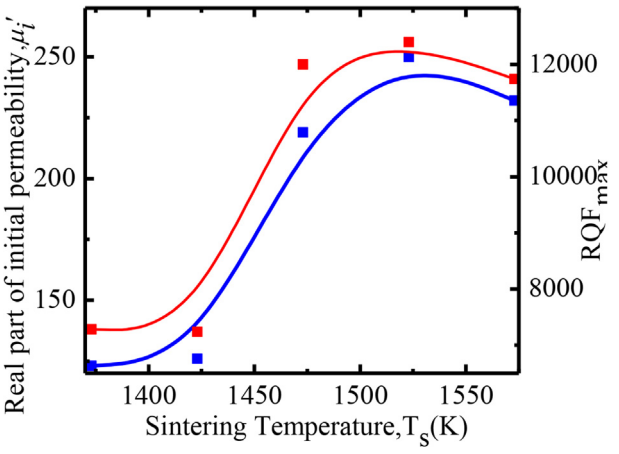

Fig. 8. Variation of μ_i' at 1 MHz and RQF with different sintering temperatures of $Li_{0.15}Ni_{0.3}Zn_{0.4}Fe_{2.15}O_4$.

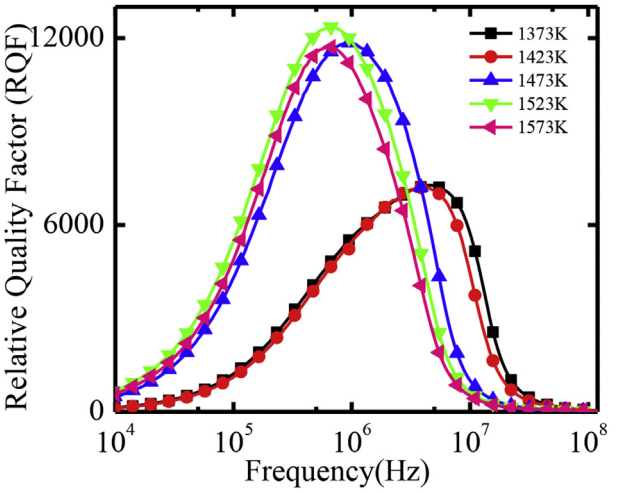

Fig. 9. The variation of RQF with different sintering temperatures of $Li_{0.15}Ni_{0.3}Zn_{0.4}Fe_{2.15}O_4$.

4. Conclusions

The XRD pattern confirms that the sample exhibits pure cubic spinel type structure. The impurity peaks are missing due to the advanced sol-gel auto combustion synthesizing method. The real part of initial permeability and microstructure are strongly dependent on T_S. Thus it can be concluded that to improve μ_i' by microstructure variation, the ferrite must be sintered at optimum temperature. Although pore and grain boundary would obstruct the movement of domain wall. The higher value of complex initial permeability is achieved at optimum sintering temperature. The $Li_{0.15}Ni_{0.3}Zn_{0.4}Fe_{2.15}O_4$ ferrite is promising for the improvement of efficient microwave absorbing materials and reducing the electromagnetic interference from electronic devices.

https://doi.org/10.1016/j.heliyon.2019.e01199

Declarations

Author contribution statement

M. A. Islam: Conceived and designed the experiments; Performed the experiments; Analyzed and interpreted the data; Wrote the paper.

M. Z. Rahaman: Conceived and designed the experiments; Analyzed and interpreted the data; Wrote the paper.

M. M. Hassan, A. K. M. A. Hossain: Analyzed and interpreted the data; Wrote the paper.

Funding statement

This work was supported by CASR, Bangladesh University of Engineering and Technology (BUET).

Competing interest statement

The authors declare no conflict of interest.

Additional information

No additional information is available for this paper.

References

[1] A.V. Malyshev, A.B. Petrova, A.N. Sokolovskiy, A.P. Surzhikov, Defects level evaluation of LiTiZn ferrite ceramics using temperature dependence of initial permeability, J. Magn. Magn. Mater. 456 (2018) 186−193.

[2] Evert Willem Gorter, Saturation magnetization and crystal chemistry of ferrimagnetic oxides. I. II. Theory of ferrimagnetism, Philips Res. Rep. 9 (1954) 295−320. https://ci.nii.ac.jp/naid/10017966827/#cit.

[3] M.K. Anupama, N. Srinatha, Shidaling Matteppanavar, Basavaraj Angadi, Balaram Sahoo, B. Rudraswamy, Effect of Zn substitution on the structural and magnetic properties of nanocrystalline $NiFe_2O_4$ ferrites, Ceram. Int. 44 (5) (2018) 4946−4954.

[4] A. Goldman, Modern Ferrite Technology, Van Nostrand Reinhold, New York, 1990.

[5] Katie Jo Sunday, Mitra L. Taheri, NiZnCu-ferrite coated iron powder for soft magnetic composite applications, J. Magn. Magn. Mater. 463 (2018) 1−6.

https://doi.org/10.1016/j.heliyon.2019.e01199

[6] Sonia Gaba, Ashok Kumar, Pawan S. Rana, Manju Arora, Influence of La^{3+} ion doping on physical properties of magnesium nanoferrites for microwave absorption application, J. Magn. Magn. Mater. 460 (2018) 69−77.

[7] N. Okasha, M. Mohsen, Ahmed I. Ali, Optimization of physical properties of Ag-Li nanoferrites via the facile citrate precursor method, J. Alloys Comp. 739 (2018) 577−585.

[8] Katie Jo Sunday, Francis G. Hanejko, Mitra L. Taheri, Magnetic and microstructural properties of Fe_3O_4-coated Fe powder soft magnetic composites, J. Magn. Magn. Mater. 423 (2017) 164−170.

[9] J. Zhan, C. Yang, X. Wang, Q. Fang, Z.T. Shi, Y. Yang, T.-L. Ren, A. Wang, Y.H. Cheng, L.-T. Liu, Stacked-spiral RF inductors with vertical nanoparticle magnetic core for radio-frequency integrated circuits in CMOS, Sensor Actuator A Phys. 195 (2013) 231−238.

[10] Shahida Akhter, M.A. Hakim, S.M. Hoque, Roland Mathieu, Per Nordblad, Glassy behavior of diluted Cu-Zn ferrites, J. Magn. Magn. Mater. 452 (2018) 261−265.

[11] B. Parvatheeswara Rao, B. Dhanalakshmi, S. Ramesh, P.S.V. Subba Rao, Cation distribution of Ni-Zn-Mn ferrite nanoparticles, J. Magn. Magn. Mater. 456 (2018) 444−450.

[12] M.A. Islam, Mehedi Hasan, AKM Akther Hossain, Enhancement of initial permeability and reduction of loss factor in Zn substituted nanocrystalline $Li_{0.35-0.5\ x}Ni_{0.3}Zn_xFe_{2.35-0.5x}O_4$, J. Magn. Magn. Mater. 424 (2017) 108−114.

[13] Jo Bo Nelson, D.P. Riley, An experimental investigation of extrapolation methods in the derivation of accurate unit-cell dimensions of crystals, Proc. Phys. Soc. 57 (3) (1945) 160.

[14] AKM Akther Hossain, S.T. Mahmud, M. Seki, T. Kawai, H. Tabata, Structural, electrical transport, and magnetic properties of $Ni_{1-x}Zn_xFe_2O_4$, J. Magn. Magn. Mater. 312 (1) (2007) 210−219.

[15] A. Goldman, Handbook of Modern Ferromagnetic Materials, Kluwer Academic Publishers, Boston, U.S.A, 1999.

[16] B.D. Cullity, C.D. Graham, Introduction to Magnetic Materials, second ed., Wiley-IEEE Press, 2008.

[17] M. Nazrul Islam, AKM Akther Hossain, Enhancement of Néel temperature and electrical resistivity of Mn−Ni−Zn ferrites by Gd^{3+} substitution, J. Mater. Res. Technol. (2018).

 https://doi.org/10.1016/j.heliyon.2019.e01199

[18] S. Karimunnesa, A.K.M. Atique Ullah, M.R. Hasan, F.S. Shanta, R. Islam, M.N.I. Khan, Effect of holmium substitution on the structural, magnetic and transport properties of $CoFe_{2-x}Ho_xO_4$ ferrites, J. Magn. Magn. Mater. 457 (2018) 57−63.

[19] A.A. Momin, Roksana Parvin, AKM Akther Hossain, Structural, morphological and magnetic properties variation of nickel-manganese ferrites with lithium substitution, J. Magn. Magn. Mater. 423 (2017) 124−132.

[20] J. Smit, H.P.J. Wijn, Physical properties of ferrites, Adv. Electron. Electron Phys. 6 (1954) 69−136. Academic Press.

[21] Per Nordblad, Rajendra Mohan, Samrat Mukherjee, Structural, magnetic and hyperfine characterizations of nanocrystalline Zn-Cd doped nickel ferrites, J. Magn. Magn. Mater. 441 (2017) 710−717.

[22] S.T. Mahmud, et al., Influence of microstructure on the complex permeability of spinel type Ni−Zn ferrite, J. Magn. Magn. Mater. 305 (1) (2006) 269−274.

[23] Roksana Parvin, A.A. Momin, AKM Akther Hossain, Improvement of microstructure, initial permeability, magnetization and dielectric properties of nanocrystalline $LixCu_{0.1}Co_{0.1}Zn_{0.8-2x}Fe_{2+x}O_4$, J. Magn. Magn. Mater. 401 (2016) 760−769.

 https://doi.org/10.1016/j.heliyon.2019.e01199